Design of a Pd-Au Nitrite Reduction Catalyst by Identifying and Optimizing Active Ensembles

Hao Li[1,‡], Sujin Guo[2,‡], Kihyun Shin[1], Michael S. Wong[2,*], and Graeme Henkelman[1,*]

[1] Department of Chemistry and the Oden Institute for Computational Engineering and Sciences, The University of Texas at Austin, 105 E. 24th Street, Stop A5300, Austin, Texas 78712, USA

[2] Department of Civil and Environmental Engineering, Nanosystems Engineering Research Center for Nanotechnology-Enabled Water Treatment, Department of Chemical and Biomolecular Engineering, Department of Chemistry, and Department of Materials Science and Nano Engineering, Rice University, 6100 S. Main Street, Houston, Texas 77005, United States

[‡] These authors contributed equally.

*Corresponding Authors:

mswong@rice.edu (M.S.W.);

henkelman@utexas.edu (G.H.);

ABSTRACT

Nitrate (NO_3^-) is a ubiquitous contaminant in groundwater that causes serious public health issues around the world. Though various strategies are able to reduce NO_3^- to nitrite (NO_2^-), a rational catalyst design strategy for NO_2^- removal has not been found, in part because of the complicated reaction network of nitrate chemistry. In this study, we show, through catalytic modeling with density functional theory (DFT) calculations, that the performance of mono- and bi-metallic surfaces for nitrite reduction can be rapidly screened using N, N_2, and NH_3 binding energies as reactivity descriptors. With a number of active surface atomic ensembles identified for nitrite reduction, we have designed a series of "metal-on-metal" bimetallics with optimized surface reactivity and a maximum number of active sites. Choosing Pd-on-Au nanoparticles (NPs) as candidate catalysts, both theory and experiment find that a thin monolayer of Pd-on-Au NPs (size: $\sim 4 \pm 0.5$ nm) leads to high nitrite reduction performance, outperforming pure Pd NPs and the other Pd surface compositions considered. Experiments show that this thin layer of Pd-on-Au has a relatively high selectivity for N_2 formation, compared to pure Pd NPs. More importantly, our study shows that a simple model, based upon DFT-calculated thermodynamic energies, can facilitate catalysts design relevant to environmental issues.

Keywords: Nitrite reduction; density functional theory; catalyst design; ensemble effect; metal-on-metal structure.

1. INTRODUCTION

Nitrate (NO_3^-) is one of the most dangerous contaminants in groundwater, causing serious public health risks around the world.[1–9] One of the most important issues is that NO_3^- can easily be converted into nitrite (NO_2^-), causing cancer, hypertension, and blue baby syndrome.[10] Therefore, many regions, including the United States, have strict regulations on the maximum contaminant level (MCL) for N to less than 10 mg/L. To remove nitrate and nitrite, a number of methods have been developed,[11] including ion exchange,[12] biological treatment,[13] reverse osmosis,[8] and electrodialysis.[14] However, these methods have some drawbacks, leading to their limited application. In particular, ion exchange leads to secondary waste which needs to be subsequently retreated by other methods;[11] biological treatment requires long startup times for biomass growth;[13] reverse osmosis and electrodialysis require additional resources and operation steps.[15] Therefore, heterogeneous catalytic treatment has emerged as a promising nitrate and nitrite removal alternative due to its quick startup and lower requirements for secondary waste treatment.[16,17] In recent years, nitrite reduction has been studied on metallic systems with and without an active substrate or oxide support.[18–26] Experiments have shown that catalytic nitrite reduction can lead to two selective reactions, the formation of dinitrogen (N_2) or ammonia (NH_3). However, due to the difficulty of *in situ* characterization of reaction sites and the unknown activity contribution from the metal or the support, it is not clear which

factors determine the activity and selectivity of the catalyst. This question remained unaddressed until a recent study by Shin et al.[15] Using theoretical and experimental methods, they found that on a Pd surface, the selectivity of nitrite reduction was determined by specific experimental conditions: a H^*-rich environment promotes the formation of NH_3, while a nitrite-rich environment promotes N_2 formation. Very recently, we found that as compared with pure Pd and Au, PdAu alloy nanoparticles (NPs) possess enhanced activity for nitrite reduction, with the Pd-Au alloy ensemble having excellent resistance to sulfide poisoning.[27] This result shows that better catalysts exist, and consideration should not be limited to monometallics. However, due to the complexity of the reaction network for nitrite reduction, to the best of our knowledge, a rational catalyst design strategy has not been used to optimize catalysts for this reaction.

To address the common goals among the communities of theoretical modeling, catalytic chemistry, and environmental science, we aim to address the issue of nitrite removal by designing new and effective environmental catalysts for this reduction. Here, instead of calculating a set of detailed kinetic pathways, we focus on developing a model that can be used to estimate the activity of a given catalytic surface. Validated by previous well-characterized experimental results, we found that the catalytic properties of both mono- and bi-metallics for nitrite reduction can be evaluated using the calculated N, N_2, and NH_3 bindings as the reaction descriptors. We find that a "metal-on-metal" structure optimizes both the surface activity and the number of the active sites. Selecting Pd-on-Au

NPs for a more detailed study, both our theory and experiment found that a thin Pd layer on Au [Pd$_{1monolayer}$/Au(111)] leads to high nitrite reduction activity and selective N$_2$ formation, as compared to pure Pd and other Pd surface coverages on Au.

2. METHODS

2.1 Computational and Modeling Methods

All calculations were performed using the VASP code. The generalized gradient approximation (GGA) method with the Perdew−Burke−Ernzerhof functional was used to describe electronic exchange and correlation.[28] The projector augmented-wave method was used to describe the core electrons.[29] Kohn−Sham wave functions were expanded in a plane wave basis with 400 eV energy cutoff to describe the valence electrons.[30] Geometries were considered converged when the forces on each atom fell below 0.05 eV/Å. A (3×3×1) Monkhorst−Pack k-point mesh was used to sample the Brillouin zone.[31] Spin polarization was tested and used when necessary, such as the calculations of single H, O, and N species in vacuum, and all the calculations on Ni(111). Entropic corrections were applied to gas phase species with the temperature of 298 K.

Each catalytic surface was modeled as slab with a four-layer, (3×3) unit cell. A vacuum layer of at least 12 Å separated periodic images of the slab. The bottom two atomic layers were kept fixed in bulk positions; the topmost two layers were allowed to relax. Our

previous studies show that a four-layer model has similar results to a five-layer model and so we did not consider thicker slabs in this study.[32] Given that the (100) surface is found to be inactive for nitrite reduction;[33] has higher surface energy;[34] and under-coordinated sites (*e.g.*, edge and corner) have negligible catalytic contribution on relatively large NP,[35] only the (111) surfaces were modeled in this study. Random alloy slabs were modelled by randomly mixing two elements with a given composition. For each composition, more than fifteen random geometries were generated. All binding sites were sampled from these surfaces. The lattice constant for each slab were calculated according to the Vegard's law and the bimetallic composition.[36] Since previous liquid phase studies have shown that solvation effects only slightly shift the relative energies and do not change the general trends of both the kinetics and thermodynamics for many reactions,[37,38] this effect was not included in our calculations. The completed modeling details and important coordinates can be found in the **Supporting Information**. All the binding energies E_b were calculated using

$$E_b = E_{tot} - E_{slab} - E_{ads}, \quad (1)$$

where E_{tot} is the energy of the system, E_{slab} is the energy of a bare slab, and E_{ads} is the energy of the adsorbate in vacuum. To evaluate the stability of the metal-on-metal structures, segregation energies E_{seg} were calculated using[39–41]

$$E_{seg} = E_{swap} - E_{tot}, \quad (2)$$

where E_{tot} is the total energy of the system, E_{swap} is the total energy of the system with the topmost core element being swapped onto the surface. Both the bare and N-absorbed systems were considered for these calculations.

2.2 Experimental Methods

2.2.1 Materials

Tetrachloroauric(III) acid (HAuCl$_4$·3H$_2$O, 99.99%), tannic acid (C$_{76}$H$_{52}$O$_{46}$, >99.5%), potassium carbonate (K$_2$CO$_3$, >99.5%), palladium(II) chloride (PdCl$_2$, 99.99%), trisodium citrate (Na$_3$C$_6$H$_5$O$_7$, >99.5%), hydrochloric acid (HCl, 1 M), and sodium nitrite (NaNO$_2$, 99.7%) were purchased from Sigma-Aldrich. Nessler's reagent (K$_2$HgI$_4$) was obtained from Fisher. Hydrogen gas (99.99%) was purchased from Airgas. A stock solution of the Griess reagent was prepared by dissolving 0.1 g of N-(1-naphthyl)ethyl-enediamine dihydrochloride, 1.0 g of sulfanilamide, and 2.94 mL H$_3$PO$_4$ in 100 mL DI water, such that the final concentrations were 0.1wt% N-(1-naphthyl)ethyl-enediamine dihydrochloride, 1wt% sulfanilamide, and 5% H$_3$PO$_4$.

2.2.2 Catalysts Synthesis

Monometallic colloidal Pd and Au NPs were synthesized through a tannic acid-sodium citrate co-reduction method.[42,43] To synthesize Au NPs, 0.05 g tannic acid, 0.018 g

K_2CO_3, and 0.04 g trisodium citrate were dissolved in 20 mL of water. In a second flask, 200 mL of $HAuCl_4$ solution (0.127 mol/L) was dissolved in 79.8 mL of water. Both solutions were heated to 60 ℃, and the first solution was added to the second under vigorous stirring. The color of the resultant sol immediately changed from pale yellow to reddish-brown, suggesting the formation of Au NPs. The solution was then heated to boiling and maintained boiling for 2 min and removed from the heat source. The sol was then diluted with DI water to 100 mL and left to cool overnight to room temperature before being stored in refrigerator. The Pd NPs were prepared in the same manner, except that the Au salt precursor solution was replaced by a palladium salt solution (12 mL of H_2PdCl_4 solution (2.49 mM) diluted in 68 mL of H_2O) and the boiling time was increased to 25 min. The solution color changed gradually from light-yellow to coffee-brown, which is the indicative color of Pd NPs.

Bimetallic Pd-on-Au NPs were prepared by adding, then subsequently reducing, the Pd salt precursor in the as-synthesized Au NPs solution with hydrogen gas. Utilizing the magic cluster model,[44] we calculated the specific volumes of 2.49 mM H_2PdCl_4 sol needed to add in the Au NPs sol for various surface coverages (sc%) on the Au NP. To prepare Pd-on-Au NPs with Pd surface coverages of 10, 50, 100, and 300 sc%, corresponding Pd solution volumes of 0.276, 1.38, 2.748, and 10.536 mL were added dropwise to 60 mL of the Au sol under vigorous stirring. The mixture was stirred at ~600 rpm for an additional

10 min followed by H_2 gas bubbling at a flow rate of $\sim$100 mL min^{-1} through the liquid for 15 min.

2.2.3 Characterization

The synthesized catalysts samples were well characterized in previous studies with transmission electron microscopy (TEM), inductively coupled plasma-atomic emission spectroscopy and X-ray absorption spectroscopy.[43,45,46] In this study, TEM images of NPs were obtained using a JEOL 2010 transmission electron microscope operating at an accelerating voltage of 200 kV. The particle size distribution was calculated by counting at least 200 particles by Image J software.

2.2.4 Catalytic Nitrite Reduction Experiments

Nitrite reduction was performed in a screw-cap Amber bottle (250 mL) sealed with a Teflon-silicone septum as a semi-batch reactor. A magnetic stirrer, DI water and colloidal NPs were placed in the reactor such that the final liquid volume was 99.5 mL. The amount of NPs added to keep the total Pd amount was 0.365 mg-Pd/L in each reactor. For example, the amount of Pd-on-Au NPs were 30, 6, and 3 mL for 10sc% Pd-on-Au NPs, 50sc% Pd-on-Au NPs, and 100sc% Pd-on-Au NPs, respectively. The catalyst solution was then bubbled simultaneously with hydrogen gas (100 mL/min, serve as reductant) and carbon

dioxide gas (100 mL/min, to buffer the solution to a pH value ~5.5) for 15 min. The

bubbling step was to reduce the catalyst surface and purge the oxygen out of the reactor as

well as make sure the reaction was in CO_2-buffered water and under a H_2 headspace. The

catalytic reactions were conducted at room temperature under constant stirring (600 rpm)

with sealed batch reactor. The $NaNO_2$ solution (0.5 mL, 10 mg/mL of NO_2^-) was injected

to start the reaction, such the initial NO_2^- concentration was 50 mg NO_2^-/L (50 ppm).

Aliquots of the reaction fluid (~1 mL) were periodically withdrawn *via* a stainless-steel

needle of a 5 mL syringe.

Similar with previous studies,[38,47] nitrite ions were analyzed using the Griess reagent

and ammonia concentrations were measured using Nessler's reagent. In a typical testing

step for nitrite, the Griess reagent solution (0.2 mL), a nitrite-containing solution (0.2 mL),

and water (1.6 mL) were mixed together and kept in room temperature for 10 min. The

absorbance at 540 nm of the colored solution was measured via UV-vis spectroscopy, and

the NO_2^- concentration was determined in the 0 to 2.0 ppm range using a standard curve.

The ammonia testing was very similar with nitrite testing step, except using the Nessler's

reagent instead of the Griess reagent.

The observed reaction rate constant k_{obs} (with unit of min^{-1}) was calculated by

assuming pseudo first-order dependence on nitrite concentration (H_2 gas was calculated in

excess),

$$-\frac{d\,C_{NO_2^-}}{dt} = k_{obs}C_{NO_2^-}, \quad (3)$$

where $C_{NO_2^-}$ is the concentration of nitrite and t is the reaction time.

In this study, we assumed that most of the N_2O can be rapidly and completely reduced to N_2,[48] and therefore we considered N_2 and NH_4^+ to be the final products. The reaction selectivities were calculated by:

$$S_{NH_3} = \left(\frac{C_{NH_4^+}}{C_0 - C}\right) \times 100\%, \quad (4)$$

$$S_{N_2} = 100\% - S_{NH_3}, \quad (5)$$

where S_{NH_3} and S_{N_2} are the selectivity of NH_3 and N_2 formation, $C_{NH_4^+}$ is the molar concentration of NH_4^+, C_0 and C represent the initial and final molar concentrations of NO_2^-, respectively.

3. RESULTS AND DISCUSSION

3.1 Nitrite Reduction Pathways

According to a previous combined theoretical and experimental study,[15] nitrite reduction with hydrogen as the reducing agent starts with the highly spontaneous redox reaction that forms NO^* from nitrite (**Figure 1**). Then NO^* can either proceed dissociative (initially forming N^*) or associative (initially forming NOH^* or HNO^*) mechanisms.[49] The association mechanism leads to NH_3 formation selectivity due to the multiple available

pathways for hydrogenation (**Figure 1**, green pathways). In contrast, the formation of N_2O^* from N^* is a key step towards N_2 formation, as indicated from previous Fourier transform infrared spectroscopy measurements.[49] Studies by Shin et al. found that the formation of N_2O^* are favorable from the reaction between N^*, H^*, nitrite, and water, with a significantly exothermic reaction energy (**Figure 1**).[15] Afterwards, N_2O^* is rapidly consumed to form N_2^*.[48,50] In summary, there are at least five possible reaction pathways for NH_3 formation, while only two primary pathways for N_2 formation. It can be seen from the reaction network that H^*-rich conditions provide NH_3 selectivity while high nitrite-rich conditions have N_2 selectivity, in good agreement with the previous conclusions drawn from both mono-[15] and bi-metallic[51] systems. In our modeling, we considered all these steps in reaction networks for N_2 and NH_3 formation.
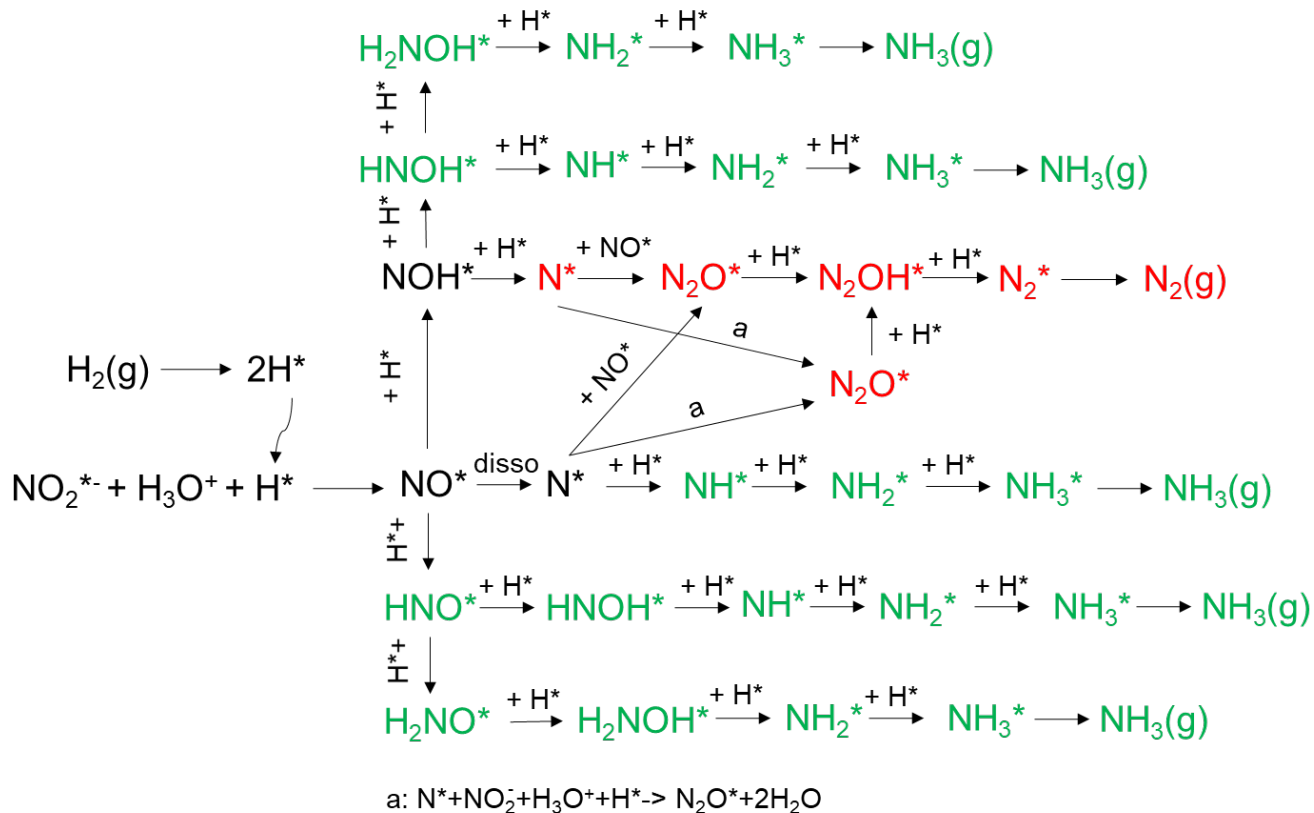
$H_2NOH^* \xrightarrow{+ H^*} NH_2^* \xrightarrow{+ H^*} NH_3^* \longrightarrow NH_3(g)$

$\uparrow + H^*$

$HNOH^* \xrightarrow{+ H^*} NH^* \xrightarrow{+ H^*} NH_2^* \xrightarrow{+ H^*} NH_3^* \longrightarrow NH_3(g)$

$\uparrow + H^*$

$NOH^* \xrightarrow{+ H^*} N^* \xrightarrow{+ NO^*} N_2O^* \xrightarrow{+ H^*} N_2OH^* \xrightarrow{+ H^*} N_2^* \longrightarrow N_2(g)$

$a \quad \uparrow + H^*$

$H_2(g) \longrightarrow 2H^* \qquad + H^* \qquad + NO^* \qquad N_2O^*$

a

$NO_2^{*-} + H_3O^+ + H^* \longrightarrow NO^* \xrightarrow{disso} N^* \xrightarrow{+ H^*} NH^* \xrightarrow{+ H^*} NH_2^* \xrightarrow{+ H^*} NH_3^* \longrightarrow NH_3(g)$

$+ H^* \downarrow$

$HNO^* \xrightarrow{+ H^*} HNOH^* \xrightarrow{+ H^*} NH^* \xrightarrow{+ H^*} NH_2^* \xrightarrow{+ H^*} NH_3^* \longrightarrow NH_3(g)$

$+ H^* \downarrow$

$H_2NO^* \xrightarrow{+ H^*} H_2NOH^* \xrightarrow{+ H^*} NH_2^* \xrightarrow{+ H^*} NH_3^* \longrightarrow NH_3(g)$

a: $N^* + NO_2^- + H_3O^+ + H^* \rightarrow N_2O^* + 2H_2O$

Figure 1. Catalytic reaction pathways for nitrite reduction. Red and green pathways represent selectivity towards N_2 and NH_3, respectively. The "*" symbols represent adsorption states. Formation of water in the reactions are not shown.

3.2 Volcano Activity Models

Previous studies show that on a Pd(111) surface, nitrite reduction can be calculated using reaction energies with excellent agreement to experiment.[15] Similarly, we have developed a model that estimates the reaction free energy based upon the adsorbate binding energy. The modeling details can be found in the **Supporting Information**. With the assumption that all reaction barriers follow the generalized Brønsted−Evans−Polanyi (BEP)

relationship where a lower reaction energy has a stronger driving force to reduce the reaction barrier,[52,53] it has been found that the reaction free energy constructed with this method has good agreement with experiment for evaluating the activity of reactions including hydrogenation[35,54–56] and oxygen reduction.[57,58] With the scaling relationships found on monometallics between N binding and all other adsorbate bindings (except N_2 and NH_3) (**Figure S1**), reaction free energies can be estimated as linear functions of the binding energies of N, N_2, and NH_3. **Figure 2a** and **2b** show the calculated volcano activity plots for the N_2 and NH_3 formation pathways, with the rate-limiting step, G_{max}, plotted as the contours. Interestingly, it can be seen that trends in G_{max} of the two reactions are similar, and that the N_2 selectivity generally tends to have a slightly lower rate-limiting reaction free energy than NH_3. This is consistent with a previous conclusion on Pd surfaces that N_2 formation pathways have lower reaction energies than NH_3.[15] This also suggests that for the same binding energies, both selectivities are limited by the same reaction steps. It can be seen from our two contour plots, that both reactions have minima with relatively low G_{max}. This is because of the two different mechanisms for nitrite reduction: the left minimum represents the NO dissociative pathways, while the right one represents its associative pathways. These results suggest that though the NH_3 mechanism has more potential pathways (as seen in **Figure 1**), the formation of N_2, which primarily follows the dissociative pathways, is thermodynamically favorable. It should be noted that these models consider N_2 and NH_3 binding energies: when the binding of N_2 or NH_3 are too

strong, the reactions would be rate-limited by the desorption of N_2 or NH_3. By plotting the monometallic surfaces onto the volcanos, it can be seen that the "strong binding metals" (Pt, Pd, Ir, Ni, and Rh)[59] tend to proceed *via* the dissociative pathways due to the active surface *d*-band for bond cleavage, while "weak binding metals" (Au, Ag, and Cu) tend to proceed *via* associative pathways with higher reaction energy than other elements. While the associative pathways have a slightly higher rate-limiting free energy than the dissociative pathways due to the high H_2 dissociation energy on these surfaces,[60] as well as weak adsorption of N_2O^* (**Figures S1-S4**), these volcano plots explain the low activity of pure Cu and Au NPs for room-temperature experiments.[27,51] A similar conclusion can be drawn for pure Ag (**Figure S3**). With this in mind, and also because the associative pathway promotes the typically unwanted NH_3 product,[15] the following catalyst design efforts attempts to optimize the surface reactivity through the dissociative pathways.

From the volcano activity plot we can see that Pt, Pd, Ir, Ni, and Rh bind N too strongly, while Au, Ag, and Cu bind N too weakly. Therefore, it is expected that alloying these strong and weak binding metals could provide a tuned N binding energy close to the optimal at the volcano peak. This assumption can be effective for bimetallics whose surface ensembles have good tunability for adsorbate bindings.[59] Here we find that N has good tunability on metallic surface since it binds to the 3-fold hollow adsorption site,[59,61] while N_2 and NH_3 are less influenced by alloying effects since they bind to atop sites (**Figure 2c**). Together with the results that most of the monometallics are not limited by N_2 or NH_3

desorption (**Figures 2a** and **2b**), we can rely on the N binding energy as a reaction descriptor for catalysts design.
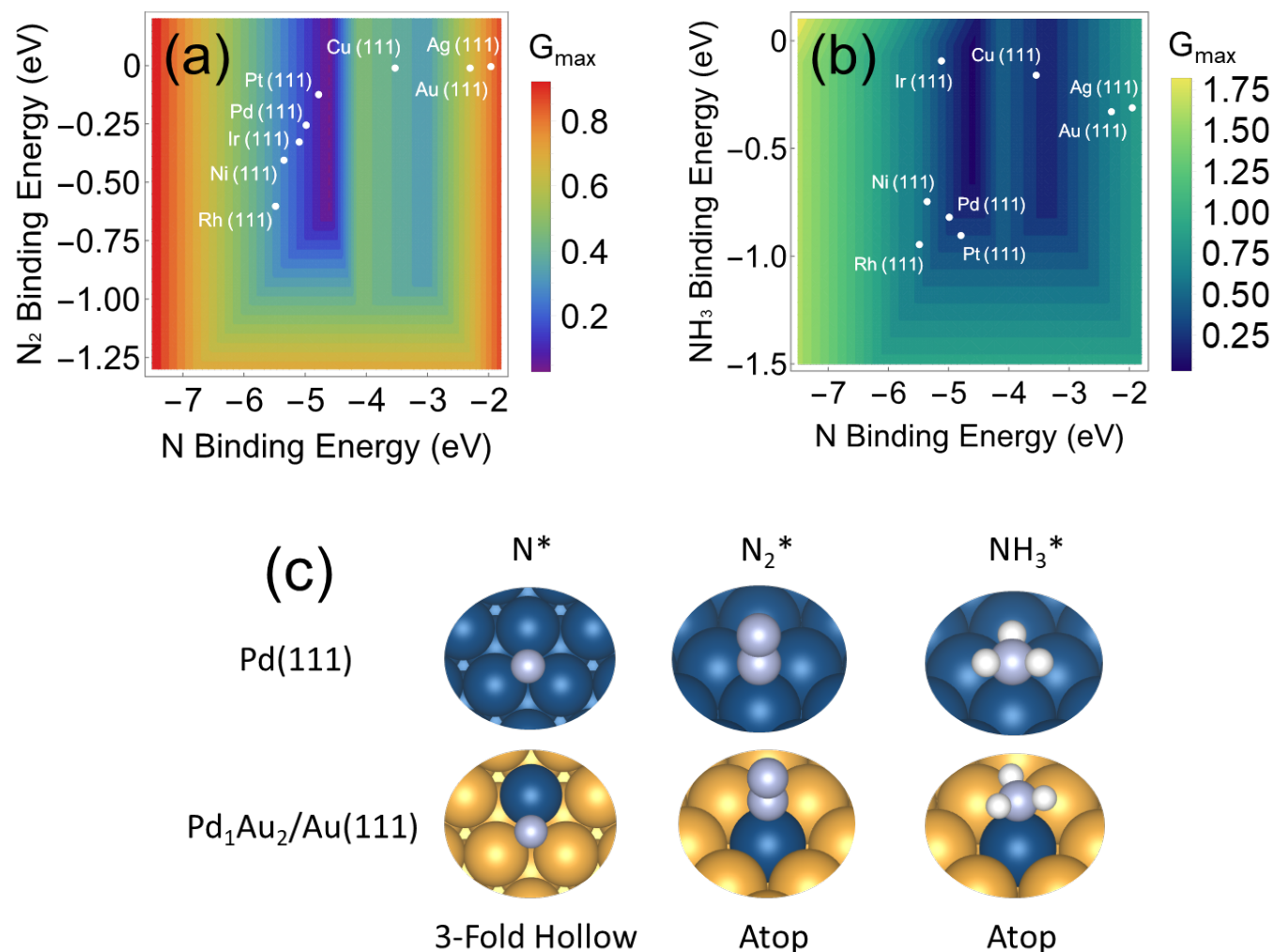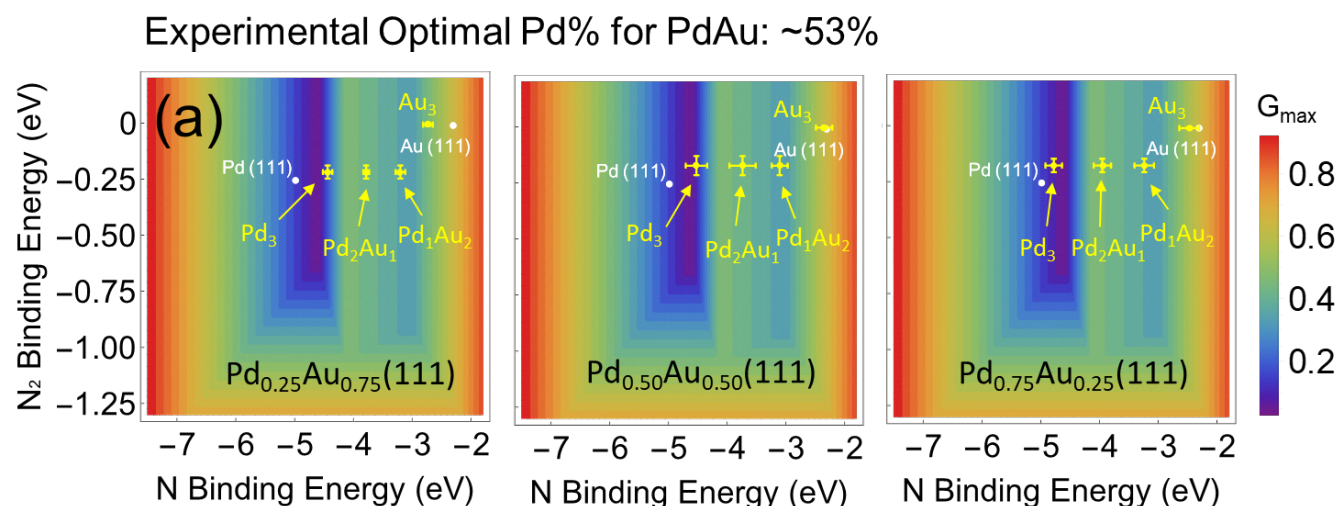

Figure 2. Volcano activity plots for nitrite reduction through (a) N_2 and (b) NH_3 formation pathways, with the plotted close-packed monometallic surfaces (white marks). (c) Optimized binding geometries of N, N_2, and NH_3 on Pd(111) and a Pd_2Au_1 surface three-fold triatomic ensemble. Blue, gold, and purple spheres represent Pd, Au, and N, respectively.

3.3 Model Validation and Active Ensemble Identification

Before being used for new catalyst design, the volcano activity plot was determined by two previous experiments. Seraj et al.[27] and Guy et al.[51] respectively synthesized and characterized PdAu and PdCu random alloy nanostructures with varying compositions and tested them for nitrite reduction. Since these nanocatalysts were tested without an active substrate, the reactivity was primarily determined by the surface reactivity of the metal catalysts. **Figure 3a** and **3b** shows the volcano activity plots with the binding energies on the triatomic ensembles (X_3, X_2Pd_1, X_1Pd_2, and Pd_3, where X=Au or Cu) at Pd_xAu_{1-x} and Pd_xCu_{1-x} (x=0.25, 0.50, and 0.75), respectively. Here we focus on the three-fold triatomic ensemble since it is the primary repeat unit for characterizing adsorbate binding through a single bond (**Figure 2b**).[27,32,35,55,56,58,59] On the random alloy models, Pd_3 is always the most active ensemble, for both PdAu and PdCu alloys. However, due to electronic and strain effects, only the Pd_3 sites on the $Pd_{0.50}Au_{0.50}$(111) and the $Pd_{0.75}Cu_{0.25}$(111) alloy can reach the peak of the volcano, indicating that a Pd% around 50% and 75% respectively on PdAu and PdCu would lead to optimized nitrite reduction activity, as compared to other compositions. This is in excellent agreement with previous experiments showing that optimal catalysts with Pd% in PdAu and PdCu respectively are 53% and 80% for nitrite reduction.[27,51] With the supposition that NH_3 selectivity has similar contour trends and can

be tuned by the hydrogen and nitrite concentrations in the experiments,[15] selectivity towards NH_3 is not discussed further.

Interestingly, it can be seen that there is a synergic interplay among the ensemble, ligand, and strain effects for tuning the N binding energy on alloy surfaces in the Pd-based alloys. First, the pure Pd ensemble is identified as having the highest nitrite reduction activity, showing the importance of the pure Pd ensembles. Secondly, due to the ligand effect from charge transfer between Pd and Au/Cu and the strain effect from the different lattice constants between Pd and Au/Cu, the N binding energies of the Pd_3 sites can reach the optimal region of the volcano (**Figure 3c** and **3d**). Most importantly, these previous well-characterized experimental results help to validate our model by directly comparing the active surface ensembles and the optimal random alloy compositions, showing that our model can predict experimental results.
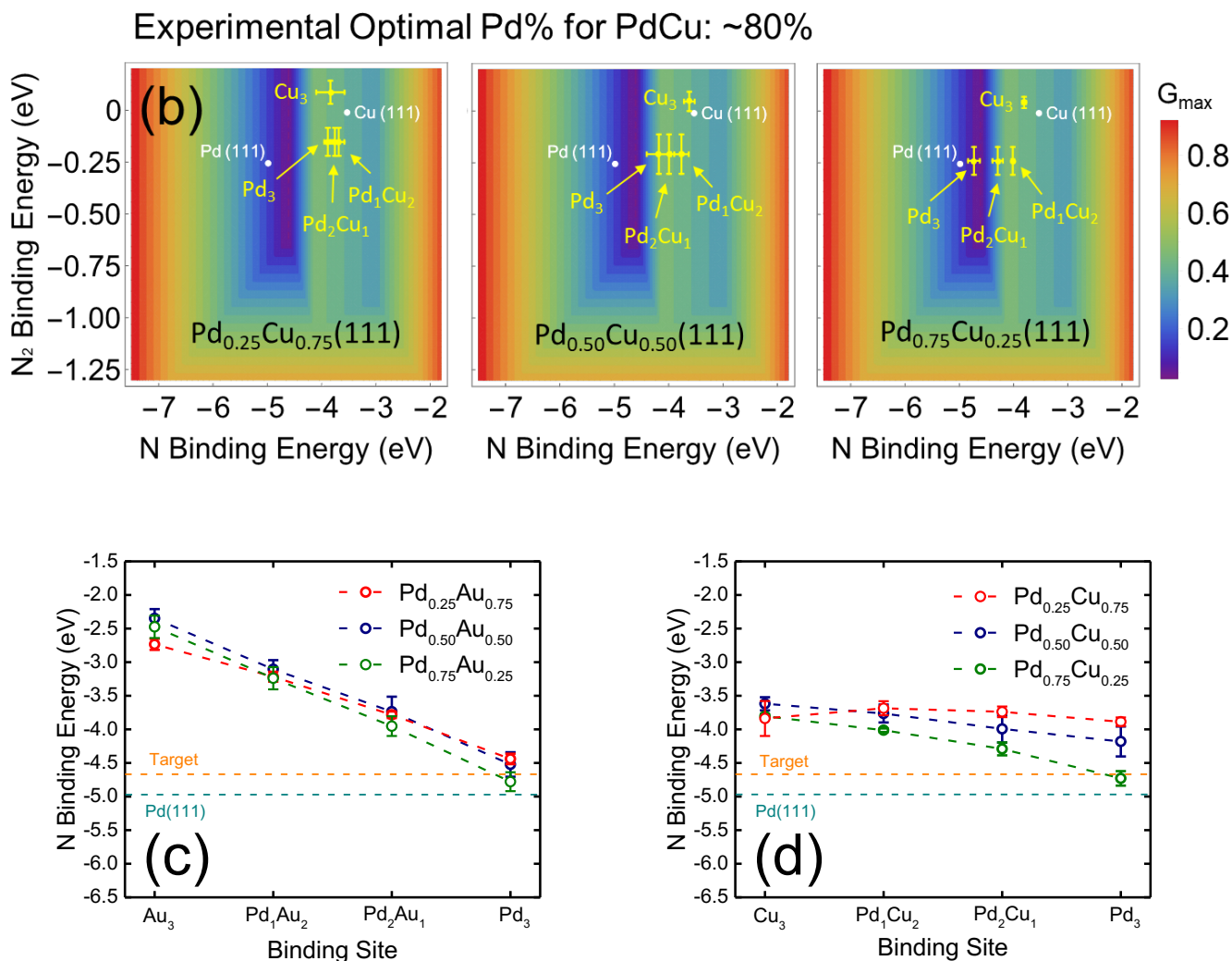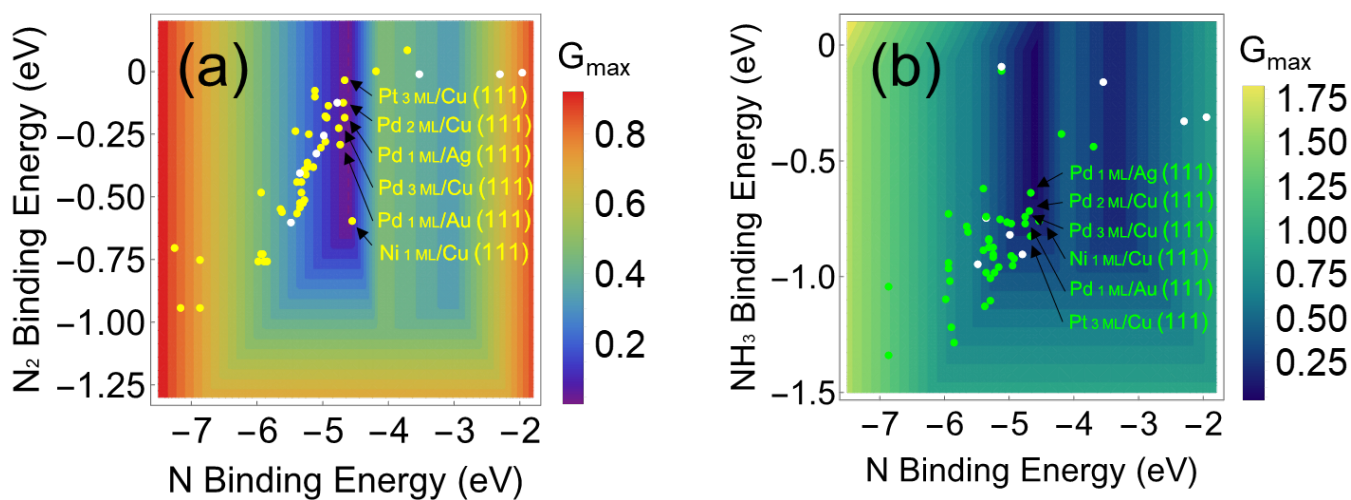
Figure 3. Predictions of nitrite reduction at triatomic ensembles on (a) PdAu and (b) PdCu random alloy surfaces. The experimental determined optimal Pd% in PdAu and PdCu alloy structures can be found in Refs.[27,51]. (c, d) Tuning the N binding energy at the triatomic ensemble of PdAu and PdCu. The orange dashed line represents N binding with the optimal activity as indicated by the volcano plot. The error bars indicate variations from ten sampled binding sites among more than fifteen randomly generated alloy geometries.

3.4 Optimizing and Maximizing the Most Active Ensembles: Design of Metal-on-Metal Catalysts

The model evaluation with random alloys indicates that the volcano model can be used for further predictions on complicated catalytic surfaces. Compared to Au, Ag, and Cu, those strong binding metals are closer to the target binding energy for high catalytic activity. Therefore, we propose that these surfaces can be tuned by substituting a sublayer element in the structure through electronic and strain effects. This strategy has been proven effective for catalyst design of hydrogen evolution,[41] oxygen reduction,[39,40] and CO oxidation.[41] Meanwhile, X-on-Y (or core@shell-like) bimetallic could provide a maximized number of active site on the catalytic surface (*e.g.*, the Pd_3 ensemble, as indicated above), which could further increase the overall activity of a catalyst. Here, we modeled a series of X-on-Y structures with X as the strong binding metal (Pd, Pt, Ir, Rh, and Ni) and Y as the weak binding metal (Au, Ag, and Cu) (**Figure 4**). For each bimetallic considered, the thickness of a shell was varied as 1, 2, and 3 monolayers (MLs), which respectively represent a thin, medium, and thick X element on a Y substrate (**Figure 4e**). Since adsorbate binding on $Ni_{1ML}/Au(111)$ and $Ni_{1ML}/Ag(111)$ results in a significant surface distortion, these two structures were not considered further. The theoretical activity of our catalysts were screened by calculating their N, N_2, and NH_3 binding energies. **Figure 4a-4c** shows that at least six of the screened catalysts are able to reach the target activity from the volcano plot [$Pd_{3ML}/Cu(111)$, $Pd_{2ML}/Cu(111)$, $Pd_{1ML}/Ag(111)$, $Pt_{3ML}/Cu(111)$,

Pd$_{1ML}$/Au(111), and Ni$_{1ML}$/Cu(111)]. Interestingly, most of these candidates are Pd surface catalysts, showing that Pd is a tunable metallic for N binding. Additionally, it can be seen that most of these optimized catalysts have relatively weak N$_2$ binding but stronger NH$_3$ binding, suggesting facile N$_2$ desorption and higher N$_2$ formation selectivity on these structures.

To evaluate the stability of these candidate catalyst, their segregation energies were calculated by swapping one of the topmost substrate element atoms onto the surface (**Figure 4d**).[39,40,62] It can be seen, thermodynamically, that surface segregation is expected on adsorbate-free surfaces from the negative segregation energies. However, with the adsorption of N, only the Pd$_{2ML}$/Cu(111) and Pd$_{3ML}$/Cu(111) surfaces have negative segregation energies. Therefore, it is expected that under mild conditions (*e.g.*, room temperature), a fully adsorbate-covered surface, and kinetically-controlled synthesis,[63–65] the four remaining catalysts should be stable during nitrite reduction.
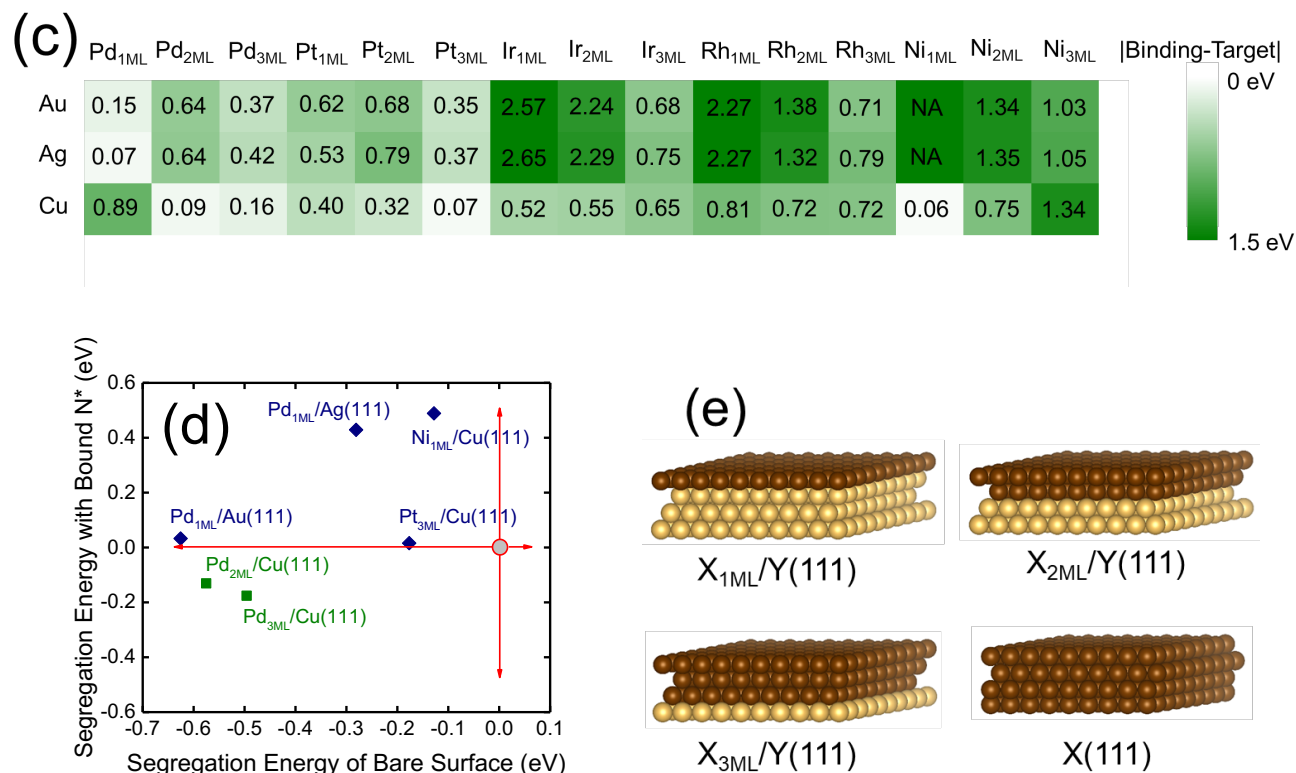
(c)	Pd$_{1ML}$	Pd$_{2ML}$	Pd$_{3ML}$	Pt$_{1ML}$	Pt$_{2ML}$	Pt$_{3ML}$	Ir$_{1ML}$	Ir$_{2ML}$	Ir$_{3ML}$	Rh$_{1ML}$	Rh$_{2ML}$	Rh$_{3ML}$	Ni$_{1ML}$	Ni$_{2ML}$	Ni$_{3ML}$
Au	0.15	0.64	0.37	0.62	0.68	0.35	2.57	2.24	0.68	2.27	1.38	0.71	NA	1.34	1.03
Ag	0.07	0.64	0.42	0.53	0.79	0.37	2.65	2.29	0.75	2.27	1.32	0.79	NA	1.35	1.05
Cu	0.89	0.09	0.16	0.40	0.32	0.07	0.52	0.55	0.65	0.81	0.72	0.72	0.06	0.75	1.34

|Binding-Target|
0 eV — 1.5 eV

Figure 4. Volcano activity plots of X-on-Y (X=Pd, Pt, Rh, Ir, and Ni; Y=Au, Ag, and Cu) catalysts through the (a) N$_2$ and (b) NH$_3$ formation pathways. (c) Matrix showing the surfaces with function quantified by the |N binding - target binding|. (d) Calculated segregation energies with and without adsorbed N* on the X-on-Y catalysts, which are predicted to possess optimal nitrite reduction activity. (e) Schematic pictures of X-on-Y catalytic models considered for DFT calculations. Brown and gold spheres represent the X and Y elements, respectively.

Among the four screened candidates, here we choose Pd-on-Au as a case study, because Pd/Au is a widely studied bimetallic that can be synthetized by a mature

kinetically-controlled method.[63–66] **Figure 5a** and **5b** shows trends of the Pd-on-Au catalysts with varying Pd thicknesses. It can be seen that the tightness of N binding to the Pd surface are in the order of $Pd_{2ML}/Au(111) > Pd_{3ML}/Au(111) \approx Pd(111) > Pd_{1ML}/Au(111)$. Also, due to the relatively strong NH_3 binding energies (**Figure 5b**), these catalysts are expected to have lower NH_3 formation selectivities. Our experiments, which we will discuss later, validate these predictions. To explain the significant difference of N bindings between Pd_{2ML} and Pd_{1ML}, the projected density of states (PDOS) of the *d*-electrons in their surface atoms were calculated, as shown in **Figure 5c**. It can be seen that there are significant differences in the peak distributions between the two surfaces. According to the *d*-band theory,[67] since the *d*-band center of Pd_{2ML} surface shifts closer to the fermi level than the Pd_{1ML}, binding to Pd_{2ML} is expected to be stronger.[58,68] Although the average Pd-Pd bond length on Pd_{1ML} is longer due to the large Au lattice constant, the electronic (ligand) effect from the sublayer induces a weakened N binding on $Pd_{1ML}/Au(111)$, reaching the target activity indicated by the volcano plot. It should be noted that compared to other PdAu alloyed ensembles, as shown in **Figure 3a**, these pure Pd sites are generally predicted to have higher activity, indicating that a Pd-on-Au structure not only optimizes the reactivity of pure Pd ensembles, but also maximizes the number of these active sites on a catalytic surface.
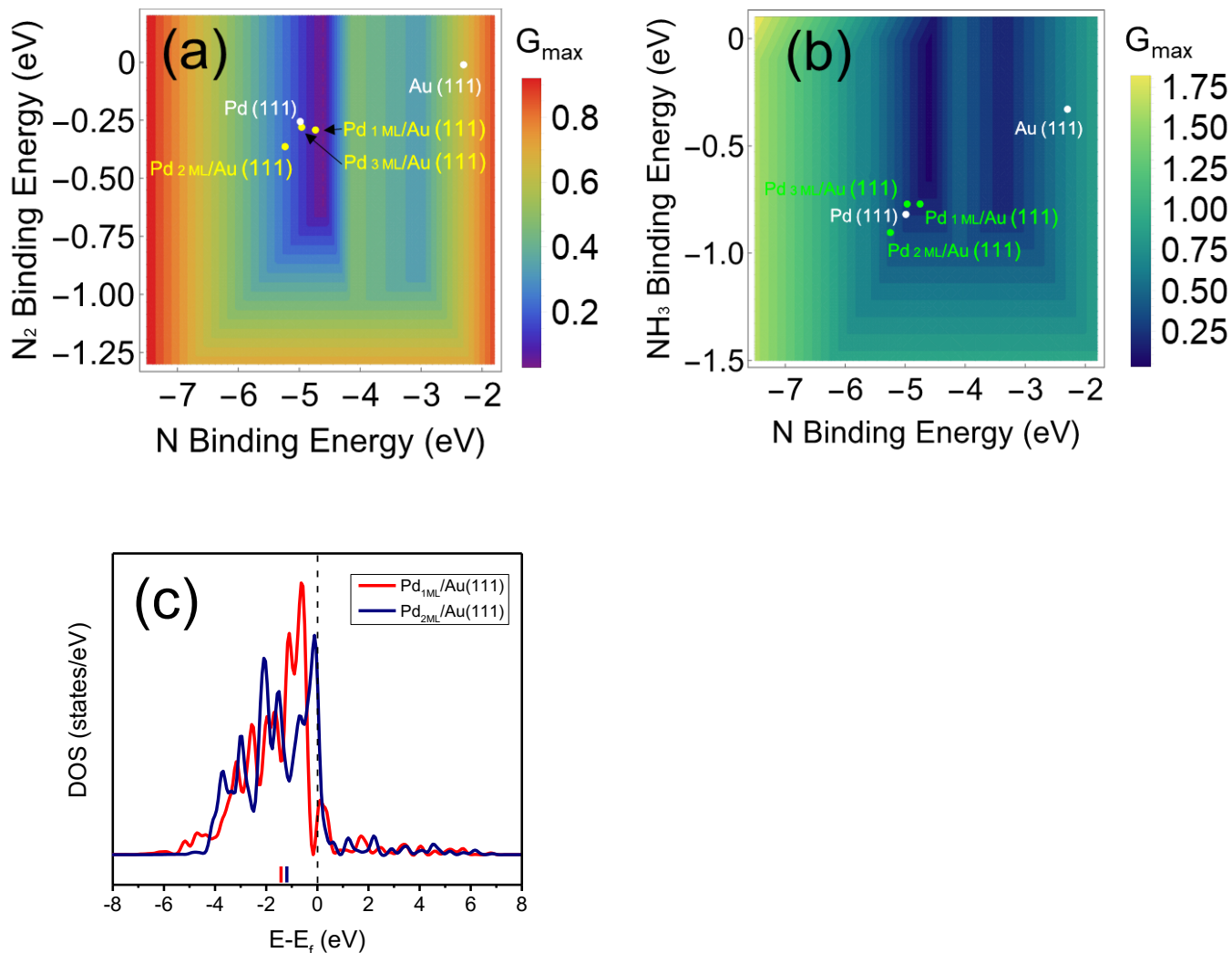
Figure 5. Volcano activity plots marked with Pd-on-Au catalysts with varying Pd layers through (a) N_2 and (b) NH_3 formation pathways. (c) Projected density of states (PDOS) of d-electrons of the surfaces of $Pd_{1ML}/Au(111)$ (red) and $Pd_{2ML}/Au(111)$ (blue). The colored horizontal bars and black dashed line represent the calculated d-band centers and Fermi energy level, respectively.

3.5 Experimental Evaluation of Pd-on-Au NPs

Here, we experimentally examine the activity and selectivity of pure Pd and Pd-on-Au NPs to validate our theoretical predictions by conducting catalytic nitrite reduction with different Pd-on-Au surface covered NPs and pure Pd NPs. Representative transmission electron microscopy (TEM) images of 100% surface coverage (sc%) Pd-on-Au NPs are shown in the inset of **Figure 6a**. The average particle sizes were almost unchanged (increasing slightly from 4.0 to 4.4 nm compared with the Au NPs, as shown in the **Supporting Information**) and the morphology of the NPs remained constant after Pd deposition (**Figure 6a**). Together with the highly miscible phase diagram of PdAu bimetallic alloys,[55] we assume that our synthesis produced a pure Pd-dominated surface on the 100sc% Pd-on-Au NPs and PdAu surface alloy on the 10 and 50sc% Pd-on-As NPs.[69–71]

The nitrite reduction activities (normalized with the quantity of surface Pd) of Pd-on-Au NPs with different Pd surface coverages are shown in **Figure 6b**. It can be seen that the surface coverage of 10% and 50% Pd outperforms the pure Pd NPs. This could be understood by the highly active pure Pd ensemble when alloyed with Au on the surface, as shown in **Figure 3a**. While the Pd surface coverage reaches 100%, the reaction kinetics have the highest activity, in excellent agreement with our theoretical prediction that a thin Pd layer could optimize the reactivity of surface Pd for nitrite reduction (**Figure 5**). We also predict that with thicker Pd surface coverage, the reactivity should decrease and become similar to that of pure Pd NPs.
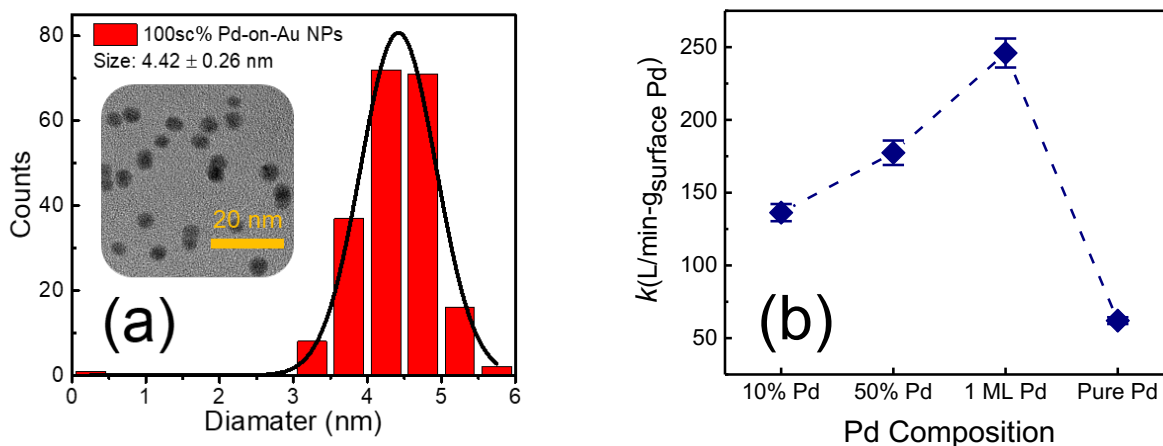
Figure 6. (a) Particle size distributions of 100sc% Pd-on-Au NPs. Each bar represents the total count of NPs with a measured diameter ± 0.26 nm. The inset shows a representative transmission electron microscope (TEM) image. TEM images of the Au NPs can be found in **Figure S5**. (b) Experimentally determined reaction kinetics (normalized by the estimated surface Pd content) of nitrite reduction on Pd-on-Au and pure Pd NPs.

Figure 7a shows that the selectivity of NH_3 with different catalysts increases as a function of % NO_2^- conversion. The NH_3 selectivity of pure Pd is higher than the Pd-on-Au NPs, in which the 50% and 100% surface coverage of Pd show less selectivity to NH_3 as the final-product. As shown in **Figure 7b**, regardless of the Pd composition, the measured selectivity to NH_3 was low at 80% NO_2^- conversion. This is in qualitative agreement with the theoretical results indicating that forming NH_3 requires overcoming high reaction free energies (**Figures 2, 4, and 5**)[15] while, the calculated selectivity to N_2 is higher than 80%. It is also clear that Pd-on-Au systems outperform the pure Pd NPs, which

is also expected from theory (**Figure 5**). That is to say, the metal-on-metal structures not only help to optimize the surface reactivity, but also tune the preference of the products.
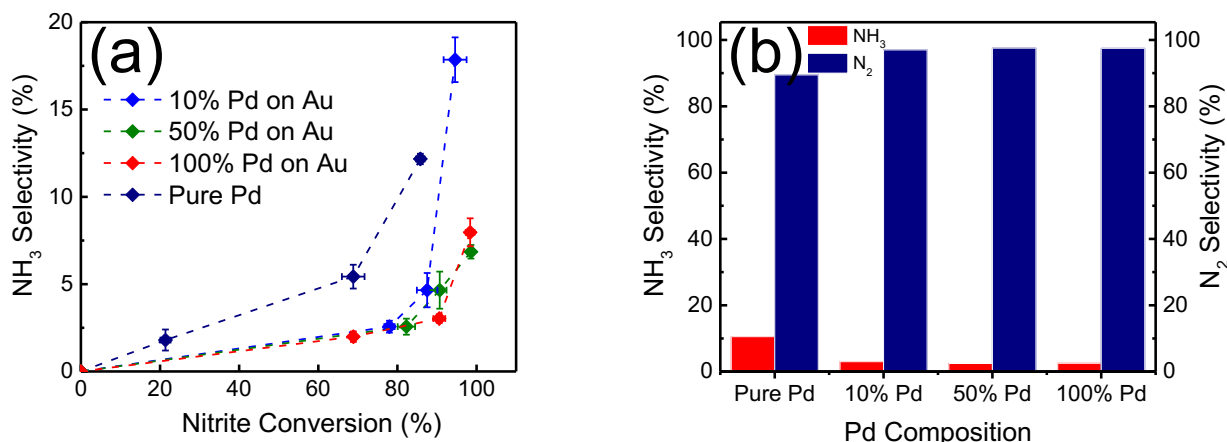

Figure 7. Experimentally determined (a) NH$_3$ selectivity at different nitrite % conversion and (b) calculated transformation product (N$_2$ and NH$_3$) selectivities at 80% nitrite conversion.

To directly compare our theoretical and experimental results, the theoretical activities of Pd-on-Au structures were estimated using the DFT-calculated reaction free energy for N$_2$ selectivity; the kinetic modeling details are provided in the **Supporting Information**. It can be seen in **Figure 8** that though there are some minor inconsistencies in the 10sc% Pd model, the overall trends for theory and experiment are similar, showing that our models are predictive for the design of catalysts for nitrite reduction in water *via* a complicated reaction network. It should be noted that this agreement is consistent with other examples of micro-kinetic modeling guiding experiments.[53] We expect that a full-

kinetic model with every energy barrier calculated would result in even higher precision. But again, due to the highly complicated reaction network for nitrite reduction, the model developed here, based on DFT-calculated thermodynamic data, is proven to possess predictive power with a low computational cost.
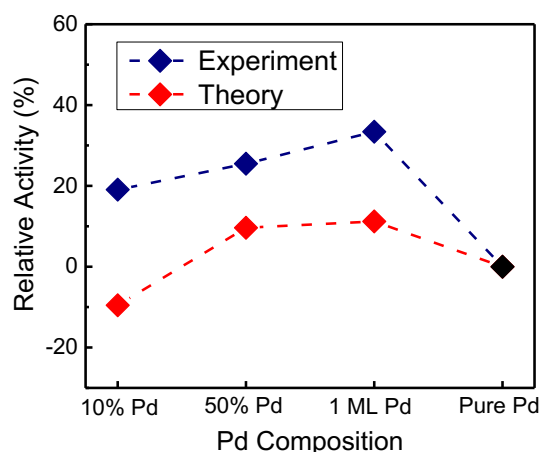

Figure 8. Trends of the experimental (blue) and theoretical (red) activities for nitrite reduction, using the activity of pure Pd as the reference. Details of the kinetic modeling can be found in the **Supporting Information**.

In our selected example, Pd-on-Au catalysts have shown promising performance for nitrite removal as well as desired N_2 formation selectivity, in excellent agreement with our theoretical expectations. Therefore, together with its validated predictive power for nitrite reduction performance on PdAu[27] and PdCu[51] alloy nanocatalysts (**Figure 3**), this model and the as-proposed catalyst design strategy show a multi-functional catalyst design, including (theoretically) identifying, (theoretically & experimentally) optimizing, and

(theoretically & experimentally) maximizing the most active surface ensembles. To the best of our knowledge, this is the first study for designing new bimetallic catalysts for addressing a pressing environmental issue with highly complicated reaction steps. We expect that other metal-on-metal structures like Pd-on-Ag, Ni-on-Cu, and Pt-on-Cu could also perform high nitrite reduction activity and good stability, as discussed in our results (**Figure 4**).

4. Conclusions

Here, we have shown that catalytic modeling can predict the performance of mono- and bi-metallic surfaces for nitrite reduction, which occurs *via* a complicated reaction network, using adsorbate binding energies as reactivity descriptors. Based upon our theoretical knowledge of ensemble, electronic, and strain effects,[59] we have designed a series of X-on-Y bimetallic structures with optimized surface reactivity and a maximum concentration of the most active ensembles identified. Considering Pd-on-Au as an example, both our theory and experiment have found that a thin Pd layer Pd-on-Au structure leads to excellent performance for nitrite reduction, as well as a high selectivity for N_2 formation. Most importantly, our study shows that the rational design of bimetallic catalyst using a knowledge of alloying effects from theory can help to address a pressing environment issue involving a complicated reaction network.

Supporting Information

Catalytic modeling methods, coordinates of important geometries, adsorption configurations of all the reaction species on monometallics, and additional characterization results.

Acknowledgements

References

(1)   Strebel, O.; Duynisveld, W. H. M.; Bottcher, J. Nitrate Pollution of Groundwater in

Western Europe. *Ecosyst. Environ. Elsevier Sci. Publ. B.V* **1989**, *26*, 189–214.

(2)   Chen, J.; Taniguchi, M.; Liu, G.; Miyaoka, K.; Onodera, S. I.; Tokunaga, T.; Fukushima, Y. Nitrate Pollution of Groundwater in the Yellow River Delta, China. *Hydrogeol. J.* **2007**, *15*, 1605–1614.

(3)   Pawar, N. J.; Shaikh, I. J. Nitrate Pollution of Ground Waters from Shallow Basaltic Aquifers, Deccan Trap Hydrologic Province, India. *Environ. Geol.* **1995**, *25*, 197–204.

(4)   Laftouhi, N. E.; Vanclooster, M.; Jalal, M.; Witam, O.; Aboufirassi, M.; Bahir, M.; Persoons, E. Groundwater Nitrate Pollution in the Essaouira Basin (Morocco). *C.R. Geosci.* **2003**, *335*, 307–317.

(5)   Elmi, A. A.; Madramootoo, C.; Egeh, M.; Hamel, C. Water and Fertilizer Nitrogen Management to Minimize Nitrate Pollution from a Cropped Soil in Southwestern Quebec, Canada. *Water. Air. Soil Pollut.* **2004**, *151*, 117–134.

(6)   Pye, V. I.; Patrick, R. Ground Water Contamination in the United States. *Science*. 1983, 713–718.

(7)   Liu, A.; Ming, J.; Ankumah, R. O. Nitrate Contamination in Private Wells in Rural Alabama, United States. *Sci. Total Environ.* **2005**, *346*, 112–120.

(8)   Schoeman, J. J.; Steyn, A. Nitrate Removal with Reverse Osmosis in a Rural Area

in South Africa. *Desalination* **2003**, *155*, 15–26.

(9) Jalali, M. Nitrate Pollution of Groundwater in Toyserkan, Western Iran. *Environ. Earth Sci.* **2011**, *62*, 907–913.

(10) Weyer, P. J.; Cerhan, J. R.; Kross, B. C.; Hallberg, G. R.; Kantamneni, J.; Breuer, G.; Jones, M. P.; Zheng, W.; Lynch, C. F. Municipal Drinking Water Nitrate Level and Cancer Risk in Older Women: The Iowa Women's Health Study. *Epidemiology* **2001**, *12*, 327–338.

(11) Kapoor, A.; Viraraghavan, T. Nitrate Removal From Drinking Water. *J. Environ. Eng.* **1997**, *123*, 371–380.

(12) Clifford, D.; Liu, X. Ion Exchange for Nitrate Removal. *J. / Am. Water Work. Assoc.* **1993**, *85*, 135–143.

(13) Lehman, S. G.; Badruzzaman, M.; Adham, S.; Roberts, D. J.; Clifford, D. A. Perchlorate and Nitrate Treatment by Ion Exchange Integrated with Biological Brine Treatment. *Water Res.* **2008**, *42*, 969–976.

(14) El Midaoui, A.; Elhannouni, F.; Taky, M.; Chay, L.; Menkouchi Sahli, M. A.; Echihabi, L.; Hafsi, M. Optimization of Nitrate Removal Operation from Ground Water by Electrodialysis. *Sep. Purif. Technol.* **2002**, *29*, 235–244.

(15) Shin, H.; Jung, S.; Bae, S.; Lee, W.; Kim, H. Nitrite Reduction Mechanism on a Pd

Surface. *Environ. Sci. Technol.* **2014**, *48*, 12768–12774.

(16) Yin, Y. B.; Guo, S.; Heck, K. N.; Clark, C. A.; Coonrod, C. L.; Wong, M. S.
      Treating Water by Degrading Oxyanions Using Metallic Nanostructures. *ACS*
      Sustain. Chem. Eng. **2018**, *6*, 11160–11175.

(17) Heck, K. N.; Guo, S.; Westerhoff, P.; Wong, M. S. Removing Nitrates and Nitrites
      through New Catalysis Chemistry. *Water Cond. Purif.* **2018**, *3*, 36–40.

(18) Hamid, S.; Kumar, M. A.; Lee, W. Highly Reactive and Selective Sn-Pd Bimetallic
      Catalyst Supported by Nanocrystalline ZSM-5 for Aqueous Nitrate Reduction.
      Appl. Catal. B Environ. **2016**, *187*, 37–46.

(19) Hamid, S.; Bae, S.; Lee, W.; Amin, M. T.; Alazba, A. A. Catalytic Nitrate Removal
      in Continuous Bimetallic Cu-Pd/Nanoscale Zerovalent Iron System. *Ind. Eng.*
      Chem. Res. **2015**, *54*, 6247–6257.

(20) Ye, T.; Durkin, D. P.; Hu, M.; Wang, X.; Banek, N. A.; Wagner, M. J.; Shuai, D.
      Enhancement of Nitrite Reduction Kinetics on Electrospun Pd-Carbon
      Nanomaterial Catalysts for Water Purification. *ACS Appl. Mater. Interfaces* **2016**,
      8, 17739–17744.

(21) Martínez, J.; Ortiz, A.; Ortiz, I. State-of-the-Art and Perspectives of the Catalytic
      and Electrocatalytic Reduction of Aqueous Nitrates. *Applied Catalysis B:*
      Environmental. 2017, 42–59.

(22) Huo, X.; Van Hoomissen, D. J.; Liu, J.; Vyas, S.; Strathmann, T. J. Hydrogenation of Aqueous Nitrate and Nitrite with Ruthenium Catalysts. *Appl. Catal. B Environ.* **2017**, *211*, 188–198.

(23) Kim, Y. N.; Kim, M. Y.; Choi, M. Synergistic Integration of Catalysis and Ion-Exchange for Highly Selective Reduction of Nitrate into N2. *Chem. Eng. J.* **2016**, *289*, 423–432.

(24) Wang, Q.; Wang, W.; Yan, B.; Shi, W.; Cui, F.; Wang, C. Well-Dispersed Pd-Cu Bimetals in TiO2 Nanofiber Matrix with Enhanced Activity and Selectivity for Nitrate Catalytic Reduction. *Chem. Eng. J.* **2017**, *326*, 182–191.

(25) Hamid, S.; Kumar, M. A.; Han, J. I.; Kim, H.; Lee, W. Nitrate Reduction on the Surface of Bimetallic Catalysts Supported by Nano-Crystalline Beta-Zeolite (NBeta). *Green Chem.* **2017**, *19*, 853–866.

(26) Perez-Coronado, A. M.; Calvo, L.; Baeza, J. A.; Palomar, J.; Lefferts, L.; Rodriguez, J. J.; Gilarranz, M. A. Selective Reduction of Nitrite to Nitrogen with Carbon-Supported Pd-AOT Nanoparticles. *Ind. Eng. Chem. Res.* **2017**, *56*, 11745–11754.

(27) Seraj, S.; Kunal, P.; Li, H.; Henkelman, G.; Humphrey, S. M.; Werth, C. J. PdAu Alloy Nanoparticle Catalysts: Effective Candidates for Nitrite Reduction in Water. *ACS Catal.* **2017**, *7*, 3268–3276.

(28) Perdew, J. P.; Burke, K.; Ernzerhof, M. Generalized Gradient Approximation Made Simple. *Phys. Rev. Lett.* **1996**, *77*, 3865–3868.

(29) Blöchl, P. E. Projector Augmented-Wave Method. *Phys. Rev. B* **1994**, *50*, 17953–17979.

(30) Kohn, W.; Sham, L. J. Self-Consistent Equations Including Exchange and Correlation Effects. *Phys. Rev.* **1965**, *140*, A1133.

(31) Monkhorst, H.; Pack, J. Special Points for Brillouin Zone Integrations. *Phys. Rev. B* **1976**, *13*, 5188–5192.

(32) Li, H.; Evans, E. J.; Mullins, C. B.; Henkelman, G. Ethanol Decomposition on Pd–Au Alloy Catalysts. *J. Phys. Chem. C* **2018**, *122*, 22024–22032.

(33) Elias, Welman C. Sujin Guo, Kimberly N. Heck, Sadegh Yazdi, Ciceron Ayala, S. Sophia Grossweiler, Josiel B. Domingos, Emilie Ringe, M. S. W. Nitrate Anions Degrade Rapidly on Indium-Decorated Pd Nanocubes. p Submitted.

(34) Foiles, S. M.; Baskes, M. I.; Daw, M. S. Embedded-Atom-Method Functions for the Fcc Metals Cu, Ag, Au, Ni, Pd, Pt, and Their Alloys. *Phys. Rev. B* **1986**, *33*, 7983.

(35) Guo, H.; Li, H.; Jarvis, K.; Wan, H.; Kunal, P.; Dunning, S. G.; Liu, Y.; Henkelman, G.; Humphrey, S. M. Microwave-Assisted Synthesis of Classically

Immiscible Ag–Ir Alloy Nanoparticle Catalysts. *ACS Catal.* **2018**, *8*, 11386–11397.

(36) Denton, A. R.; Ashcroft, N. W. Vegards Law. *Phys. Rev. A* **1991**, *43*, 3161–3164.

(37) Tripkovic, V.; Vegge, T. Potential- and Rate-Determining Step for Oxygen

Reduction on Pt(111). *J. Phys. Chem. C* **2017**, *121*, 26785–26793.

(38) Guo, S.; Heck, K.; Kasiraju, S.; Qian, H.; Zhao, Z.; Grabow, L. C.; Miller, J. T.;

Wong, M. S. Insights into Nitrate Reduction over Indium-Decorated Palladium

Nanoparticle Catalysts. *ACS Catal.* **2018**, *8*, 503–515.

(39) Zhang, L.; Henkelman, G. Tuning the Oxygen Reduction Activity of Pd Shell

Nanoparticles with Random Alloy Cores. *J. Phys. Chem. C* **2012**, *116*, 20860–

20865.

(40) Zhang, L.; Iyyamperumal, R.; Yancey, D. F.; Crooks, R. M.; Henkelman, G.

Design of Pt-Shell Nanoparticles with Alloy Cores for the Oxygen Reduction

Reaction. *ACS Nano* **2013**, *7*, 9168–9172.

(41) Zhang, L.; Henkelman, G. Computational Design of Alloy-Core@shell Metal

Nanoparticle Catalysts. *ACS Catal.* **2015**, *5*, 655–660.

(42) Heck, K. N.; Nutt, M. O.; Alvarez, P.; Wong, M. S. Deactivation Resistance of

Pd/Au Nanoparticle Catalysts for Water-Phase Hydrodechlorination. *J. Catal.* **2009**,

267, 97–104.

(43) Pretzer, L. A.; Song, H. J.; Fang, Y. L.; Zhao, Z.; Guo, N.; Wu, T.; Arslan, I.; Miller, J. T.; Wong, M. S. Hydrodechlorination Catalysis of Pd-on-Au Nanoparticles Varies with Particle Size. *J. Catal.* **2013**, *298*, 206–217.

(44) Nutt, M. O.; Heck, K. N.; Alvarez, P.; Wong, M. S. Improved Pd-on-Au Bimetallic Nanoparticle Catalysts for Aqueous-Phase Trichloroethene Hydrodechlorination. *Appl. Catal. B Environ.* **2006**, *69*, 115–125.

(45) Zhao, Z.; Arentz, J.; Pretzer, L. a; Limpornpipat, P.; Clomburg, J. M.; Gonzalez, R.; Schweitzer, N.; Wu, T.; Miller, J. T.; Wong, M. Volcano-Shape Glycerol Oxidation Activity of Palladium-Decorated Gold Nanoparticles. *Chem. Sci.* **2014**, *5*, 3715–3728.

(46) Zhao, Z.; Miller, J. T.; Wu, T.; Schweitzer, N. M.; Wong, M. S. EXAFS Characterization of Palladium-on-Gold Catalysts Before and After Glycerol Oxidation. *Top. Catal.* **2015**, *58*, 302–313.

(47) Qian, H.; Zhao, Z.; Velazquez, J. C.; Pretzer, L. A.; Heck, K. N.; Wong, M. S. Supporting Palladium Metal on Gold Nanoparticles Improves Its Catalysis for Nitrite Reduction. *Nanoscale* **2014**, *6*, 358–364.

(48) Zhang, R.; Shuai, D.; Guy, K. A.; Shapley, J. R.; Strathmann, T. J.; Werth, C. J. Elucidation of Nitrate Reduction Mechanisms on a Pd-In Bimetallic Catalyst Using Isotope Labeled Nitrogen Species. *ChemCatChem* **2013**, *5*, 313–321.

(49) Sá, J.; Anderson, J. A. FTIR Study of Aqueous Nitrate Reduction over Pd/TiO2.
Appl. Catal. B Environ. **2008**, *77*, 409–417.

(50) Jung, S.; Bae, S.; Lee, W. Development of Pd-Cu/Hematite Catalyst for Selective
Nitrate Reduction. *Environ. Sci. Technol.* **2014**, *48*, 9651–9658.

(51) Guy, K. A.; Xu, H.; Yang, J. C.; Werth, C. J.; Shapley, J. R. Catalytic Nitrate and
Nitrite Reduction with Pd-Cu/PVP Colloids in Water: Composition, Structure, and
Reactivity Correlations. *J. Phys. Chem. C* **2009**, *113*, 8177–8185.

(52) Evans, M. G.; Polanyi, M. Inertia and Driving Force of Chemical Reactions. *Trans.
Faraday Soc.* **1938**, *34*, 11.

(53) Ferrin, P.; Simonetti, D.; Kandoi, S.; Kunkes, E.; Dumesic, J. A.; Nørskov, J. K.;
Mavrikakis, M. Modeling Ethanol Decomposition on Transition Metals: A
Combined Application of Scaling and Brønsted-Evans-Polanyi Relations. *J. Am.
Chem. Soc.* **2009**, *131*, 5809–5815.

(54) García, S.; Zhang, L.; Piburn, G. W.; Henkelman, G.; Humphrey, S. M. Microwave
Synthesis of Classically Immiscible Rhodium-Silver and Rhodium-Gold Alloy
Nanoparticles: Highly Active Hydrogenation Catalysts. *ACS Nano* **2014**, *8*, 11512–
11521.

(55) Kunal, P.; Li, H.; Dewing, B. L.; Zhang, L.; Jarvis, K.; Henkelman, G.; Humphrey,
S. M. Microwave-Assisted Synthesis of PdxAu100-x Alloy Nanoparticles: A

Combined Experimental and Theoretical Assessment of Synthetic and Compositional Effects upon Catalytic Reactivity. *ACS Catal.* **2016**, *6*, 4882–4893.

(56) Piburn, G. W.; Li, H.; Kunal, P.; Henkelman, G.; Humphrey, S. M. Rapid Synthesis of Rhodium–Palladium Alloy Nanocatalysts. *ChemCatChem* **2018**, *10*, 329–333.

(57) Nørskov, J. K.; Rossmeisl, J.; Logadottir, A.; Lindqvist, L.; Kitchin, J. R.; Bligaard, T.; Jónsson, H. Origin of the Overpotential for Oxygen Reduction at a Fuel-Cell Cathode. *J. Phys. Chem. B* **2004**, *108*, 17886–17892.

(58) Li, H.; Luo, L.; Kunal, P.; Bonifacio, C. S.; Duan, Z.; Yang, J. C.; Humphrey, S. M.; Crooks, R. M.; Henkelman, G. Oxygen Reduction Reaction on Classically Immiscible Bimetallics: A Case Study of RhAu. *J. Phys. Chem. C* **2018**, *122*, 2712–2716.

(59) Li, H.; Shin, K.; Henkelman, G. Effects of Ensembles , Ligand , and Strain on Adsorbate Binding to Alloy Surfaces. *J. Chem. Phys.* **2018**, *149*, 174705.

(60) Evans, E. J.; Li, H.; Yu, W. Y.; Mullen, G. M.; Henkelman, G.; Mullins, C. B. Mechanistic Insights on Ethanol Dehydrogenation on Pd-Au Model Catalysts: A Combined Experimental and DFT Study. *Phys. Chem. Chem. Phys.* **2017**, *19*, 30578–30589.

(61) Liu, P.; Nørskov, J. K. Ligand and Ensemble Effects in Adsorption on Alloy Surfaces. *Phys. Chem. Chem. Phys.* **2001**, *3*, 3814–3818.

(62) Li, H.; Chai, W.; Henkelman, G. Selectivity for Ethanol Partial Oxidation: The Unique Chemistry of Single-Atom Alloy Catalysts on Au, Ag, and Cu(111). *J. Mater. Chem. A* **2019**, in press.

(63) Lu, C. L.; Prasad, K. S.; Wu, H. L.; Ho, J. A. A.; Huang, M. H. Au Nanocube-Directed Fabrication of Au-Pd Core-Shell Nanocrystals with Tetrahexahedral, Concave Octahedral, and Octahedral Structures and Their Electrocatalytic Activity. *J. Am. Chem. Soc.* **2010**, *132*, 14546–14553.

(64) Lee, Y. W.; Kim, M.; Kim, Z. H.; Han, S. W. One-Step Synthesis of Au@Pd Core-Shell Nanooctahedron. *J. Am. Chem. Soc.* **2009**, *131*, 17036–17037.

(65) Fang, P. P.; Jutand, A.; Tian, Z. Q.; Amatore, C. Au-Pd Core-Shell Nanoparticles Catalyze Suzuki-Miyaura Reactions in Water through Pd Leaching. *Angew. Chemie - Int. Ed.* **2011**, *50*, 12184–12188.

(66) Yang, C. W.; Chanda, K.; Lin, P. H.; Wang, Y. N.; Liao, C. W.; Huang, M. H. Fabrication of Au-Pd Core-Shell Heterostructures with Systematic Shape Evolution Using Octahedral Nanocrystal Cores and Their Catalytic Activity. *J. Am. Chem. Soc.* **2011**, *133*, 19993–20000.

(67) Hammer, B.; Nørskov, J. K. Electronic Factors Determining the Reactivity of Metal Surfaces. *Surf. Sci.* **1995**, *343*, 211–220.

(68) Li, H.; Henkelman, G. Dehydrogenation Selectivity of Ethanol on Close-Packed

Transition Metal Surfaces: A Computational Study of Monometallic, Pd/Au, and Rh/Au Catalysts. *J. Phys. Chem. C* **2017**, *121*, 27504–27510.

(69) Han, S.; Mullins, C. B. Surface Alloy Composition Controlled O2 Activation on Pd–Au Bimetallic Model Catalysts. *ACS Catal.* **2018**, *8*, 3641–3649.

(70) Evans, E. J.; Li, H.; Henkelman, G.; Mullins, C. B. Oxidative Cross-Esterification and Related Pathways of Co- Adsorbed Oxygen and Ethanol on Pd-Au. *ACS Catal.* **2019**, *9*, 4516–4525.

(71) Yu, W.-Y.; Zhang, L.; Mullen, G. M.; Henkelman, G.; Mullins, C. B. Oxygen Activation and Reaction on Pd–Au Bimetallic Surfaces. *J. Phys. Chem. C* **2015**, *119*, 11754–11762.